Solar Physics (2023) 298:17
https://doi.org/10.1007/s11207-023-02107-8

Solar Irradiance Spectra from the *Compact SOLSTICE* (CSOL) Experiment: Instrument Design, FUV Calibration, Measurements, and Comparison of the 2018 Rocket Flight

Edward Thiemann[1] · Jerald Harder[1] · Thomas Woods[1] · Martin Snow[1,2,3] · Michael Klapetzky[1] · Matthew Triplett[1] · Alan Sims[1] · Steven Penton[1] · Mitchell Furst[4]

Received: 30 May 2022 / Accepted: 4 January 2023 / Published online: 2 February 2023

Abstract
The *Compact SOLSTICE*, a compact far and mid ultraviolet (FUV and MUV) spectrograph, flew on a sounding rocket on 18 June 2018 to validate and potentially calibrate the *SOLar STellar Irradiance Comparison Experiment* (SOLSTICE) onboard the *Solar Radiation Climate Experiment* (SORCE) spacecraft. This article reports the instrument design, the calibration of the FUV channel, and the FUV irradiance measurements. Irradiance measurements are compared to SOLSTICE showing agreement within the combined instrumental uncertainties at most wavelengths, including the H Lyman-α emission at 121.6 nm. Some unexplained differences in line ratios between 130.5 nm and 147.5 nm are observed.

Keywords Solar irradiance · Spectrograph · Far ultraviolet · Instrumentation

1. Introduction

Precise knowledge of the solar spectral irradiance at far and middle ultraviolet (FUV: 115 – 180 nm and MUV: 180 – 320 nm) wavelengths is important for understanding processes on the Sun as well as planetary atmospheres. The line and continuum features of the FUV and MUV solar spectrum are determined by processes in the solar chromosphere, transition region, and, to a lesser extent, the corona, which vary with solar magnetic activity

This article belongs to the Topical Collection:
The Solar Radiation and Climate Experiment (SORCE) Mission: Final Calibrations and Data Products
Guest Editor: Thomas N. Woods

✉ E. Thiemann
thiemann@lasp.colorado.edu

1 Laboratory for Atmospheric and Space Physics, University of Colorado Boulder; 3665 Discovery Drive; Boulder, CO 80303, USA

2 South African National Space Agency, Hospital Street, Hermanus 7200, South Africa

3 Department of Physics and Astronomy, University of the Western Cape, Robert Sobukwe Road, Bellville 7535, South Africa

4 Synchrotron Ultraviolet Radiation Facility SURF III, National Institute of Standards and Technology, Gaithersburg, MD, USA

and solar rotation. This variable radiation is readily absorbed by gases common in planetary atmospheres (e.g. O_2, CO_2, O_3, CH_4), affecting both the atmospheric energy budget and composition. This broad importance of the FUV and MUV solar spectral irradiance motivated NASA to include the *SOLar-STellar Irradiance Comparison Experiment* (SOLSTICE) instruments on the *Upper Atmospheric Research Satellite* (UARS, 1991 – 2005: Rottman, Woods, and Sparn, 1993; Woods, Rottman, and Ucker, 1993) and the *Solar Radiation and Climate Experiment* (SORCE, 2003 – 2020: Rottman, 2005; Snow et al., 2005a) spacecraft mission.

The SORCE/SOLSTICE instrument measured solar irradiance from 115 to 320 nm with a beginning-of-mission accuracy of 2 – 6% and a stability of 0.3% per year using stellar calibrations (McClintock, Snow, and Woods, 2005; Snow et al., 2005b). Routine stellar operations were greatly curtailed in 2011, when SORCE operations were adjusted to accommodate limitations of batteries, which were operated years beyond their design life, compromising the long-term uncertainty knowledge (Snow et al., 2022). In an effort to improve the accuracy of the SOLSTICE data record between 2011 and 2020, a rocket-based calibration under-flight measurement was made on 18 June 2018, using the *Compact SOLSTICE* (CSOL) instrument. Additionally, the CSOL instrument provides a technologically feasible, miniaturized version of the SOLSTICE instrument to provide both FUV and MUV spectra at a resolution of 0.4 nm over the 115 – 308 nm spectral range. This article describes the CSOL instrument design and calibration, and it compares spectral irradiance measurements between SORCE/SOLSTICE and CSOL. The emphasis in this article is on the FUV channel, because the rocket-flight measurement was optimized for the FUV spectrum signal levels. See Section 2.3 for details.

2. Instrument Design and Specifications

2.1. Opto-Mechanical Design

CSOL is a two-slit spectrograph, where the relative slit location enables the measurement of a broad spectral range with a single grating and detector. One slit is optimized for measuring the MUV spectrum (hereafter termed the "MUV slit" and corresponding "MUV Channel"), while the second is optimized for measuring the FUV spectrum (hereafter termed the "FUV slit" and corresponding "FUV Channel"). Figure 1a shows a top view of the CSOL optics and light path. The slits are displaced in the direction perpendicular to the plane of the page, resulting in two spectral stripes at the detector, also displaced in the direction perpendicular to the plane of the page. See Figure 1b for a perspective view of the slit and spectral-stripe displacement. The angular separation of the slits in the cross-dispersion direction is optimized to cover the spectral range 115 – 308 nm with the combined channels. Figure 1c shows where the spectral-stripes fall on the detector, with the FUV channel range (115 – 247 nm) in parentheses. Filters are installed before the entrance slits for visible light rejection and order sorting. In particular, the filter on the MUV slit is optimized to suppress the grating second order, which would otherwise fall on the grating first order location (shown with green in Figure 1c). A single baffle is located inside the instrument to block diffraction of third-order and higher from both the FUV and MUV channels and to minimize the influence of visible radiation. The MUV channel third-order location is shown in pink in Figure 1c; the FUV channel third-order is overlapping, but omitted for clarity. Wavelengths above 230 nm on the FUV channel have a $<$ 115 nm second-order contribution. This article only considers

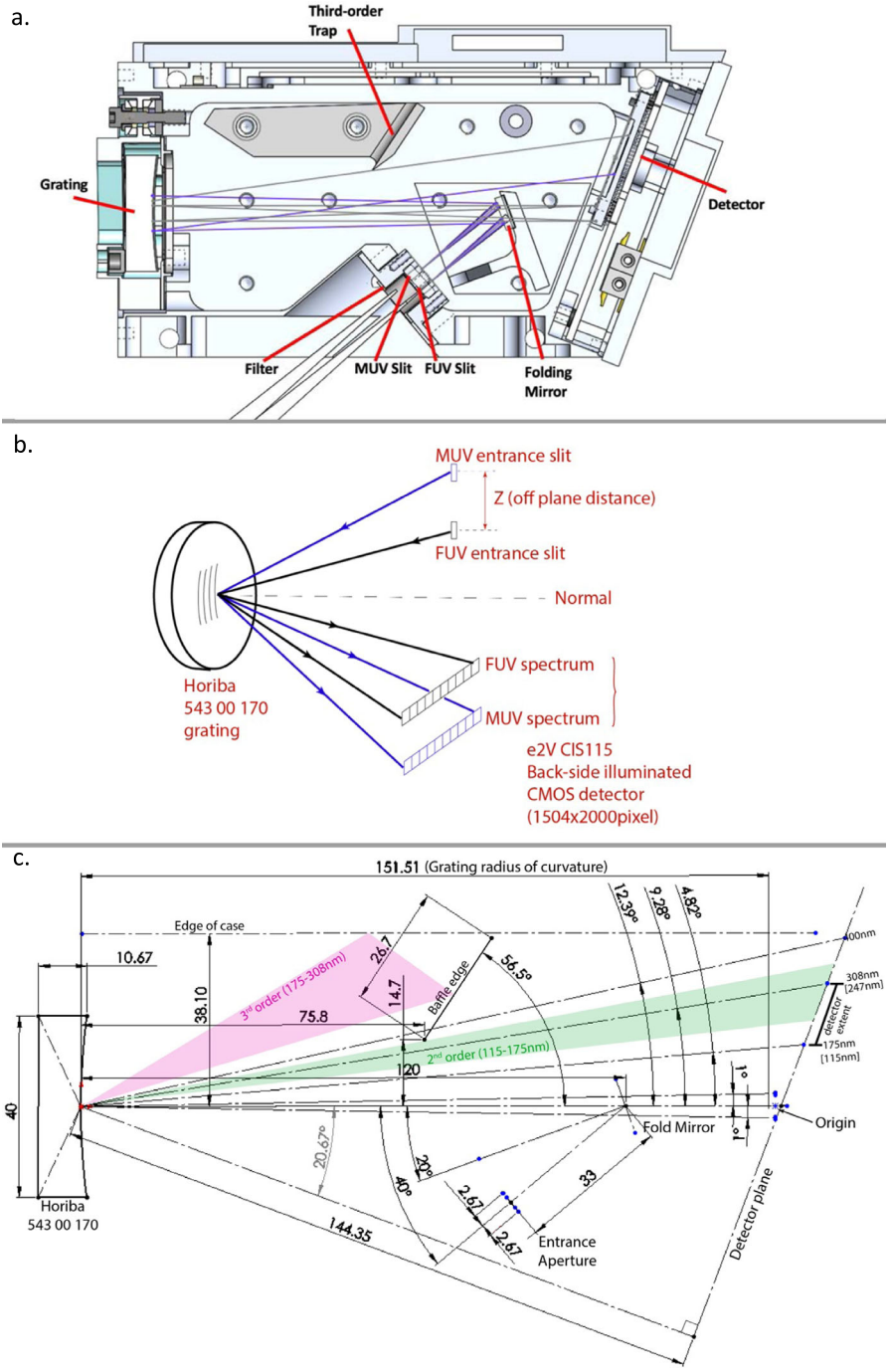

Figure 1 CSOL optical geometry. **(a)** computer-aided-design (CAD) model cross-section showing the orientation of the CSOL optics with ray traces overlayed. The instrument is approximately 180 mm×80 mm. **(b)** Cartoon showing the relative displacement of the entrance slits and corresponding spectral-stripes on the detector. **(c)** Detailed schematic of optical-component positions. Units are in mm.

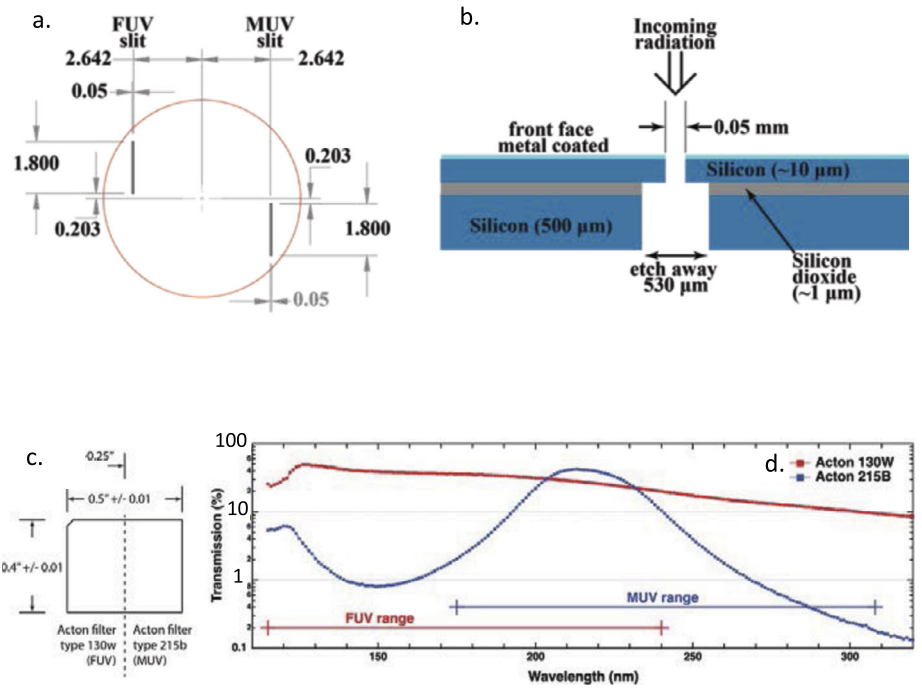

Figure 2 Slit plane and filter details. **(a)** The CSOL slit dimensions and relative orientation. Units are in mm. **(b)** Slit plane cross-section with dimensions and materials. **(c)** Filter schematic. **(d)** Filter transmission curves.

FUV wavelengths below 200 nm, so no attempt is made to correct for this higher-order contribution. Locations of where the opposite orders fall can be estimated from Figure 1c by using the line marked "origin" as the axis of symmetry. This light falls on the folding mirror mount (missing the mirror) and surrounding case, which are all coated black. Since the detector substrate is silicon, it is sensitive to stray-light contamination particularly for the very weak FUV continuum near Ly-α (H I 121.6 nm). The interior of the CSOL spectrometer chamber is painted black and has been vacuum baked to remove organic contaminants.

It is important to note that the CSOL instrument does not have any moving parts, thereby improving reliability, stability, and longevity for potential future longer-term spacecraft-based applications.

CSOL weighs 2.523 kg and is $22.2 \times 11.7 \times 9.3$ cm^3. This should be compared to SORCE/SOLSTICE, which weighed 18 kg and was $84.6 \times 38.7 \times 18.3$ cm^3. Note that SORCE/SOLSTICE had the capability to perform on-orbit calibrations using stellar irradiance measurements, while CSOL (in this current design) does not have this capability.

2.2. Entrance Slit Specifications

The entrance slit is constructed on a single 25.4 mm disk constructed using photolithography on a silicon-on-insulator wafer. Figure 2a shows the slit dimensions and relative displacement [units are mm]; the red circle is for illustrative purposes. The wafer consists of two layers of amorphous silicon separated by an insulating layer of silicon dioxide, as shown by

the cross-sectional diagram in Figure 2b. The silicon dioxide layer is needed in the manufacturing process. The Sun-facing side of the slit disk is Aluminum coated to 900 nm thickness to inhibit visible/infrared radiation from penetrating into the spectrometer. The major advantage of these slits is that the 10 μm thick edges of the slit produce a straighter edge profile and lower scatter than any mechanically produced slit because of the relative thinness of the slit-plane (10 μm for an etched slit vs. 250 – 2500 μm for a mechanically produced slit). A 530 μm cavity is etched out behind each slit to prevent light scattering, with the front-side etched to produce a 1.8 mm × 0.05 mm slit. The slit dimensions were measured by the National Institute for Standards and Technology (NIST) to be 1.8 mm × 0.04985 mm. The first and zeroth grating diffraction orders are very closely spaced, so the zeroth-order light beam propagates back out of the entrance slits. A black disk is attached to the back-side of each slit to suppress retro-reflections of zeroth-order light back towards the grating.

2.3. Filter Specifications

The CSOL instrument requires significant rejection of visible light since the FUV/MUV signals are very weak relative to the visible portion of the spectrum. Specifically, the FUV/MUV contribution to the total solar irradiance is only 1% (Rottman, 1988). To help reduce the amount of visible light making it through the entrance slit, a custom bandpass filter, manufactured by Acton Inc., is mounted in front of the entrance slit. Figure 2c shows the filter dimensions. The filter consists of two standard bandpasses manufactured by Acton, one on each half of the MgF_2 filter substrate, such that they are mounted in front of separate slits. Details of the filter can be found at www.actonoptics.com/products/. The 130W bandpass is in the optical path of the FUV channel. It has a peak transmission of 49% near 130 nm with near perfect suppression of higher grating orders due to the 115 nm cutoff wavelength of MgF_2. The 130W bandpass transmission function is shown in Figure 2d with a red curve. The 215B bandpass is in the optical path of the MUV channel. The 215B bandpass has a peak transmission of 42% near 215 nm and drops to 0.18% near 308 nm. The second grating order is reduced by up to a factor of 50. Second-order suppression is also aided by the rapid increase of the solar spectral intensity with increasing wavelength from the FUV to MUV spectral regions (e.g. Woods et al., 2009).

During testing, it was discovered the transmission of the MUV channel filter is approximately 2× too high, preventing measurements of both the FUV and MUV solar-irradiance spectra with the same detector integration time. The integration time during the rocket-flight was optimal for the FUV spectrum, but much of the MUV spectrum was saturated and unusable. A command was sent during the flight to reduce the CSOL integration period to acquire good MUV spectra, but this command was not ultimately accepted. Therefore, Sections 3 and 4 focus primarily on the FUV channel. Future implementations of this instrument should decrease the transmission of the MUV channel filter by approximately 50%.

2.4. Grating Specifications

The instrument uses a Horiba 543 00 170 holographic grating optimized for 175 – 400 nm. The grating size is 40 mm × 40 mm and focuses with an F/# of four. The grating has a ruling density of 580 mm^{-1}, near-linear dispersion (0.1 mm nm^{-1}), and medium spectral resolution (0.5 nm). It is based on an aberration-corrected Type IV grating design (Hayat et al., 1975), optimized for flat-field and imaging spectrographs

The MUV slit is oriented such that grating-$\alpha = -1.0^\circ$ and produces a spectrum ranging from 175 nm to 308 nm on the detector. The FUV slit is oriented such that grating-$\alpha = +1.0^\circ$

producing a spectrum from 114.8 to 247 nm. The cross-dispersion-direction center lines of the grating, detector, and slit plane are all in the same plane. Given this, the displacement of the slits in the cross-dispersion-direction (equivalent to the long-slit direction) prevents the FUV and MUV spectra from overlapping at the detector. In other words, defining the FUV slit to be on the top-half of the slit plane, its spectrum will be on the bottom-half of the detector (while the MUV spectrum will be on the top-half of the detector). Note, the symmetry of the grating and slit orientation results in the grating zeroth order reflecting towards the opposite slit. The backside of the slit plane has a black cover, with openings for the slits, to reduce stray-light from the zeroth-order retro-reflection.

2.5. Detector Characteristics

CSOL uses an e2v CIS115 back-side illuminated CMOS image sensor with a custom LASP-built interface board. The detector has 7 μm square pixels in a 1504 × 2000 pixel array. The detector is mated with a thermoelectric cooler (TEC), and it is capable of operations down to about −15 °C for calibration purposes when backed by a cold finger. A cold finger was not used during the rocket-flight, and stand-alone cooling with the TEC during the rocket-flight maintained a temperature of about +15 °C, thereby increasing the detector dark-current. The manufacturer specification sheet quotes a dark-current rate of 20 e- pix^{-1} sec^{-1} at 20 °C. The sensor and associated electronics consume 2 W, with the TEC adding an additional 7 W. Total mass of the detector is 127 g. The analog-to-digital conversion gain is set up to give 1.8 data numbers per electron, with a top-count of 65,535 data numbers or 36,408 e-, which is slightly above the full-well capacity of 33,000 e-. The detector integration time is ten seconds for both the radiometric calibrations and rocket-flight.

2.6. Instrument Focus

Instrument focus was achieved by first finding the optical center-line and then adjusting the grating until a pair of input beams, symmetric about the center-line, come into focus at the detector. Specifically, the center of the optical system was found by aligning a laser through the entrance slit to a mechanically mounted pinhole mask in front of the grating. Once the center-line was determined, the mask was removed and the laser was rotated in the dispersion direction at ± one degree offset angles relative to the center-line. If the system was not in focus, the images of the laser spots on the detector were displaced and blurred. The grating was shimmed in a forward or backward direction along the optical axis until the one-degree offsets converge with the center of the optical system and reach a minimum separation as measured at the detector location. In practice, the CSOL instrument was mounted in a four-axis tip/tilt/x–y displacement stage, and the optical axis of the instrument was found from cruciform scans by displacing the instrument using either a Hg 254.36 nm line from a penray lamp, and we also used a tunable tripled Ti-sapphire laser from the NIST *Spectral Irradiance and Radiance Responsivity Calibrations using Uniform Sources* (SIRCUS: Brown et al., 2004) laser system on loan to LASP at several MUV wavelengths to verify uniformity of the focus. The light sources were then focused onto a multi-mode fused silica fiber that feeds an off-axis parabolic mirror thereby giving a collimated beam that fills both the FUV and MUV entrance slits. This procedure worked very well for the MUV, but the absence of usable line sources in the FUV made this procedure unusable. For the purpose of focusing, we assume that the focus is unchanged for the fully reflective CSOL optical system.

2.7. Wavelength Scale, Dispersion, and Resolution

The wavelength assignment is relatively easy for the MUV portion of the spectrum, since reliable laser lines from the NIST SIRCUS system can provide multiple MUV wavelengths from the tunable tripled Ti:sapphire laser system. This laser system has the advantage of being very intense, so the strong signals can overcome the attenuation of the CSOL MUV filter. A monochromatic laser-calibration source is achieved by focusing the laser beam onto a multimode fiber optic that then feeds an off-axis parabola. Since the front surface of the CSOL pre-filter and entrance slit are reflective, the reflected laser beam propagates back down the fiber to a beamsplitter to where a photodiode can monitor the light intensity. This greatly eases the alignment of the light source to the CSOL optical path.

A preliminary MUV wavelength scale was estimated from laser lines at 226.333, 237.305, 265.129, 280.075, and 295.219 nm, and 254.36 nm from a mercury lamp. The centroid of each of these laser lines is located on the CSOL detector and fitted with a fourth-order polynomial. 226 nm is the shortest wavelength that can be used with the laser system. A platinum lamp was used for the initial FUV wavelength calibration standard (NIST, 2018). The final wavelength calibration for the instrument was determined from the June 2018 rocket-flight and was set to match the wavelength scale of the higher resolution SOLSTICE instrument, which has a relative accuracy and stability of 0.001 nm and 0.002 nm at FUV and MUV wavelengths, respectively (Snow et al., 2005a).

With the given wavelength versus pixel-number polynomial calibration (completed by comparison to SORCE/SOLSTICE), the dispersion can be readily calculated by differentiation of this polynomial in units of nm pixel^{-1}. The dispersion shows deviations from linear of about 10% for both the FUV and MUV channels, but since the grating was designed for wavelengths greater than 175 nm, additional curvature appears in the dispersion. Furthermore, for radiometric calibration and comparison studies highly accurate wavelength alignment and slit function convolution require a precise measure of the dispersion. Figure 3 shows the dispersion for the FUV and MUV channels. In this graph, the dispersion appears as a negative number because wavelength decreases with increasing pixel number. At 175 nm, the CSOL detector has 0.007 mm wide pixels and an MUV channel dispersion of 0.066389 nm pixel^{-1} giving a dispersion of 9.484 nm mm^{-1}; about 2% lower than the manufacturer's quoted dispersion of 9.698 nm mm^{-1}.

The instrument spectral resolution can be computed from the values shown in Figure 3, given a 0.04958 mm wide FUV entrance slit. For example, the spectrograph passes a wavelength band of 0.476 nm near 175 nm.

3. Instrument Calibration and Uncertainty

3.1. Measurement Equation

The fundamental measurement equation for solar irradiance [$E_{\mathrm{sol}}(\lambda)$] measured by CSOL is given by

$$E_{\mathrm{sol}}(\lambda) = \frac{C(M, f_L, \lambda, D, S, B, d)}{R(\lambda, \theta, \phi) t_{\mathrm{i}} \Delta\lambda} \tag{1}$$

where λ is wavelength, t_{i} is the integration time, θ and ϕ are the angular coordinates pitch and yaw, respectively, and

$$C = M f_L(M) + d(\lambda) - D - B - S(\lambda) \tag{2}$$

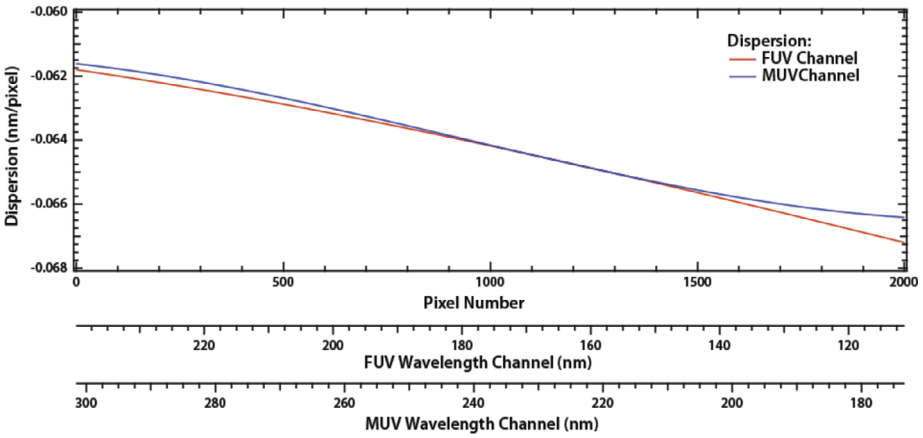

Figure 3 Instrument wavelength scale and dispersion.

are the corrected counts due to irradiance derived from the measured counts $[M]$ by applying a linearity correction $[L]$ and then adding depleted counts $[d]$ and subtracting dark counts $[D]$, background stray-light $[B]$, and scattered-light $[S]$;

$$R(\lambda, \theta, \phi) = T_{\mathrm{F}}(\lambda)\epsilon(\lambda, \theta, \phi)QE(\lambda)FOV(\theta, \phi)A \tag{3}$$

is the instrument net-response-function determined by the product of the filter transmission $[T_{\mathrm{F}}]$, the grating efficiency $[\epsilon]$, detector quantum efficiency $[QE]$, field-of-view factor $[FOV]$, and slit area $[A]$. R was measured directly at the *NIST Synchrotron Ultraviolet Radiation Facility* (SURF) III (Arp et al., 2000) rather than being calculated from the values of its constituent terms.

3.2. NIST Synchrotron Ultraviolet Radiation Facility III

CSOL was calibrated at *Beamline* 2 of SURF III at the NIST laboratories in Gaithersburg, Maryland prior to launch from 18 – 19 April 2018 and after launch from 12 – 15 March 2019. CSOL was stored in a clean environment and unused from the period between its rocket-flight and calibration at SURF III to avoid degrading the instrument. Only the post-launch calibration data are used in this article because signal levels and calibration source characteristics were better optimized for the post-launch calibration based on lessons-learned from analyzing the pre-launch calibration.

SURF III uses an electron synchrotron with electron energies ranging in the low to mid hundreds of MeV to produce a UV spectrum with calculable irradiance having 0.1% uncertainty from 4 nm to 400 nm. This high accuracy is only achievable with direct illumination of the CSOL slits by the synchrotron radiation. As such, no optics (mirrors, gratings, filters, etc.) are placed between CSOL and the synchrotron-emission aperture during irradiance calibrations. The intense EUV emissions of the synchrotron can rapidly degrade the CSOL optics. To mitigate this, a MgF_2 window is inserted in the beam-line except for during absolute radiometric calibrations. Figure 4 shows the SURF III spectrum at the nominal calibration energy of 285 MeV. The units are in photons per second per mA synchrotron current. The photon flux at the slit is found by scaling this spectrum with the precisely known instantaneous synchrotron current, which can range from nA to hundreds of mA. Figure 5a is an

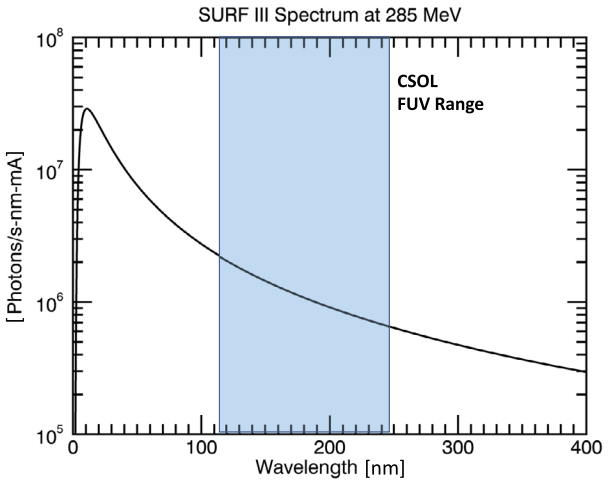

Figure 4 Example of a synchrotron spectrum at the nominal calibration energy of 285 MeV.

example CSOL measurement of a 285 MeV SURF spectrum during radiometric calibrations of the FUV channel. The dispersion direction is in the vertical direction with wavelength increasing in the upward direction. The stripe on the left is the FUV spectrum, and that on the right is the MUV spectrum.

CSOL was mounted to a two-axis (pitch and yaw) gimbal housed inside an ultra-high-vacuum chamber at the end of the beamline. The two-axis gimbal can be adjusted remotely from outside the vacuum chamber. The roll axis must be manually set from within the chamber. Because the synchrotron beam is highly parallel polarized (in the direction of the synchrotron orbital plane) and the CSOL optics (in particular the grating) are polarization-dependent, three sets of calibrations are made at different roll positions. Specifically, roll is set with the long-slit dimension oriented 0°, 90°, and −45° from vertical. The chamber can be moved both horizontally and vertically for beam translation relative to CSOL.

CSOL was precisely centered in the beam prior to calibrations. The SURF beam size at the CSOL slit location is about nine mm in diameter. The beam cross-section is so large that it illuminates both the FUV and MUV slits simultaneously, and both channels could, in principle, be calibrated simultaneously. However, it is much simpler to calculate the incident irradiance with the slit centered on the beam, and the absolute radiometric calibrations are done with the respective slit centered on the beam. Centering is achieved using a quadrant-diode position sensor attached to CSOL for alignment purposes. The translational and angular offsets between the CSOL and position-sensor bore-sights were measured at LASP prior to the SURF III calibration campaign. At SURF III, the beam is scanned in the horizontal and vertical directions over the quadrant diode to find the point of peak intensity; this is taken to be the translational center of the quadrant diode. The beam is then set to the position-sensor translational center, and pitch and yaw are adjusted until the intensity on each of the position sensor's individual quadrants are in balance, indicating alignment of the beam with the position sensor bore-sight. The translational center is then re-scanned to correct for any translational displacement during the pitch and yaw alignment. The beam is then translated to the CSOL slit centers using the pre-determined translational offsets. Corrections for the angular offset between the position sensor and CSOL are made using the measured field-of-view (FOV) correction described in Section 3.7.

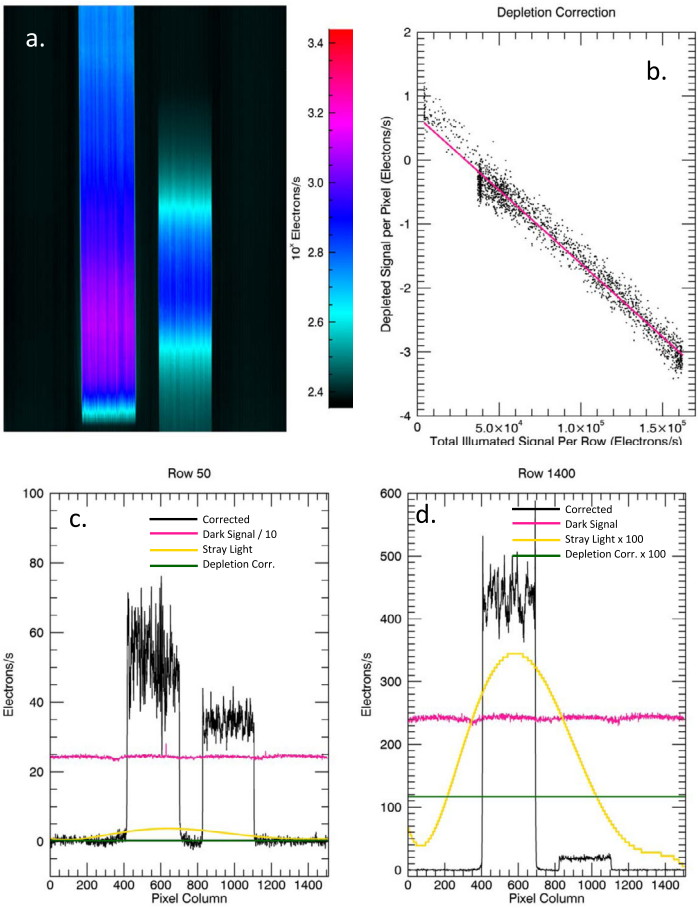

Figure 5 Offset corrections measured at SURF. **(a)** Example detector image when illuminated with a 285 MeV synchrotron beam. **(b)** Depleted counts as a function of total illuminated signal per row. **(c)** Example of the magnitudes of the dark, stray, and depleted counts to the corrected signal at Row 50 and **(d)** Row 1400.

3.3. Dark, Stray-Light, and Depletion Corrections

A typical radiometric calibration is comprised of two minutes (12 samples at ten-second integrations) of illuminated calibration followed by one minute of dark measurements to measure the dark-current contribution. The illuminated and dark samples are averaged (separately) to produce a single average illuminated image and single average dark image for each radiometric calibration. Figures 5c and 5d show example dark-current profiles for rows 50 and 1400 of the detector image in Figure 5a. Note, the dark signal in Figure 5c is divided by 10 to put it on the same scale as the other curves shown.

The stray-light contribution is also shown in Figures 5c and 5d. Stray-light is quantified for each detector row independently using polynomial fits to the dark-corrected signal away from the FUV and MUV spectral-stripes. Third- and fifth-order polynomials were used, depending on the in-band (i.e. the spectral-stripe) signal intensity. If the maximum in-band signal was below 555 e^{-} s^{-1}, then a point in-between the two stripes was included in the

fit and a fifth-order polynomial was used to approximate the stray-light. Otherwise, a third-order polynomial fit was used without a point in the middle of the stripes. Two fits are needed because it was found that scattered-light elevates the signal between the stripes, as discussed in Section 3.4, and corrupts the stray-light fit. Both fits use the same four points between the left edge and column 300, and the right edge and column 750.

A third, and relatively small, offset correction is the depletion correction that accounts for a decrease in signal in a given row that is proportional to the total illuminated signal in that row. For example, a high in-band signal on the FUV and MUV stripes will cause the signal on un-illuminated pixels in the same row to go below their expected dark value. Although small, this offset could potentially introduce non-negligible error to FUV measurements in regions of the detector where the FUV signal is faint and the MUV signal is large, and vice versa. To our knowledge, this effect has not been previously reported and it is unclear if this is a general feature in CMOS image sensors or unique to the CSOL sensor type and/or read-out electronics. The relationship between the depleted signal per pixel and total illuminated signal in a given row is highly linear, as shown in Figure 5b. The fit to these data is used to estimate the depleted counts across an entire row based on the summed signal across the FUV and MUV stripes.

3.4. Scattered Light Correction

Scattered light from the grating redistributes photons from their intended spectral location at the detector to nearby pixels according to

$$I_{\mathrm{Det}}(\lambda) = \int_{-\infty}^{\infty} I_{\mathrm{NS}}(\lambda') GDF(\lambda - \lambda') \mathrm{d}\lambda', \tag{4}$$

where I_{Det} is the photon flux at the detector, I_{NS} is the ideal photon flux at the detector if there were no grating-scatter, and GDF is the grating distribution function, which reallocates photons to regions of the detector corresponding with different wavelengths. Note, Equation 4 is a convolution. The GDF can be represented with a Lorentzian function of the form (Woods et al., 1994)

$$GDF = K\left[\frac{w^2}{(\lambda - \lambda')^2 + w^2} + A_{\mathrm{B}}(\lambda')\right], \tag{5}$$

where w is the Lorentzian half-width at half maximum, A_{B} is a background contribution due to Rayleigh scattering, and K is a constant that normalizes the GDF integral to unity. The value $[w]$ is related to the number of coherently illuminated grooves $[N]$ by

$$w = \frac{\lambda'}{\sqrt{2}\pi N}. \tag{6}$$

Snow et al. (2005a) showed that $A_{\mathrm{B}}(\lambda') = 3 \times 10^5/\lambda^5$ for the SOLSTICE gratings. N is the product of the beam-width at the grating and ruling density, $1.674 \times \lambda$, with λ in nm. The A_{B} scaling factor can vary between gratings and was not measured directly for CSOL. However, laser line measurements at 235 nm with CSOL show that the CSOL A_{B}-value is smaller than that for SOLSTICE. To establish the amount of possible error that is incurred using the larger SOLSTICE A_{B}-value for CSOL, grating-scatter calculations were made using the SOLSTICE A_{B}-value, $0.1\times$ the SOLSTICE A_{B}-value, and $0.01\times$ the SOLSTICE A_{B}-value. The spectral differences resulting from the SOLSTICE A_{B}-value versus $0.1\times$ the

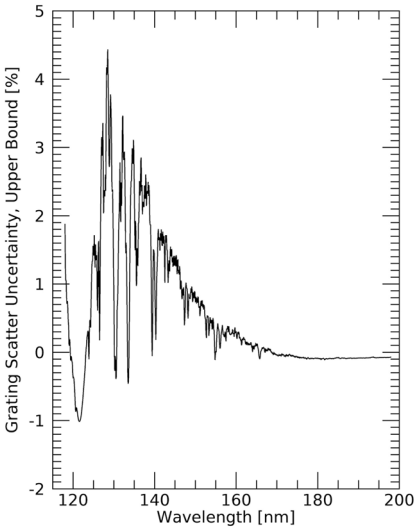

Figure 6 Estimate uncertainty in the grating-scatter correction from assuming the SOLSTICE A_B-parameter for CSOL.

SOLSTICE A_B-value has a maximum of 2.5% near 128 nm and falls below 1% at 126 nm and 139 nm. Changing the approximated A_B-value from 0.1× to 0.01× results in little further difference in the grating-scatter correction, and the difference found using the 0.01 SOLSTICE A_B-value is shown in Figure 6. As such, the CSOL A_B-value is assumed to be the same as that for SOLSTICE at a cost of a small increase in measurement uncertainty, discussed further in Section 3.8. I_{NS} is found by casting Equation 4 into a matrix equation, where GDF is a matrix. GDF^{-1} is found with the IDL Invert function, and the equation is solved algebraically. A five-bin (0.33 nm) box-car smoothing function is applied to I_{Det} prior to inversion to reduce error introduced by the numerical inversion.

If the grating-scatter correction results in a negative signal in a particular wavelength bin, the signal for this wavelength bin is set to zero. This occurs in spectral regions with a low signal-to-noise ratio (SNR) that are adjacent to steep signal gradients, such as adjacent to the H Lyman-α line, or near 127 nm, which is subjected to grating-scatter from both H Lyman-α and from the O I and Si II emissions near 130.4 nm. This occurs in less than 2% (26 of 2000) spectral bins, and all of these bins occur between 117.05 nm and 128.58 nm. These bins are considered spurious and excluded from the irradiance analysis. The implication of this is that the grating-scatter uncertainty shown in Figure 6 is likely an underestimate in regions of low SNR.

The grating also scatters light in the cross-dispersion direction, an example of which is shown in Figure 7a, where dark, depletion, and stray-light corrected data are shown in black, and the red curves are a fit to the cross-dispersion scatter. The cross-dispersion scatter is fit using pixels on the outside of the two spectral stripes. The pixels between the two spectral-stripes are not used for fitting because scatter in this region is a superposition of scatter from both spectral-stripes. The cross-dispersion scatter is assumed to be symmetric about each spectral-stripe, hence cross-dispersion scatter in-between the two stripes is estimated by "reflecting" the fitted scatter to the inner spectral-stripe edge. For the example shown in Figure 7a, data from pixel column 316 to 406 are fit to a Lorentzian function (i.e. the same-shaped function used to model scattered-light in the dispersion direction). The fit is then used to estimate the scatter from pixel column 0 to 416. To estimate the scatter in-between the spectral-stripes and scattering from one stripe to the other, the fit array is reversed and

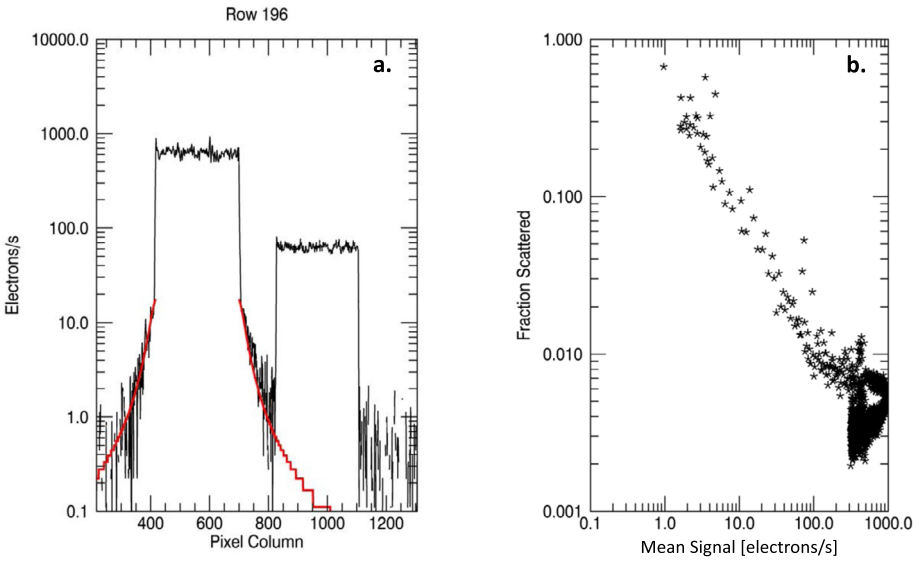

Figure 7 Cross-dispersion grating-scatter. **(a)** Example showing cross-dispersion scatter and fits (in *red* used to correct the scatter. **(b)** Dependence of the cross-dispersion scatter magnitude (in fractional units) on the average signal, showing cross-dispersion scatter becomes important at low signal levels.

shifted to pixel 701. The estimated scatter is subtracted from the data to remove the cross-dispersion scattered-light, including light scattered from one stripe to the other. In order to preserve photons, the scattered-light signal is integrated and added back to its respective spectral-stripe. For this example, the integrated scattered signal is 0.6% of the integrated non-scattered signal. The cross-dispersion scatter correction becomes spurious at low signal levels as is evident by an unphysical increase in the estimated fraction of signal scattered with decreasing signal, as shown in Figure 7b. As such, a value of 2889 e^{-} s^{-1} is used as the threshold above which the cross-dispersion correction is applied.

The cross-dispersion scatter can impact the accuracy in two ways. First, particularly at low signal levels, the fraction of signal scattered becomes large; and second, scattered-light from the MUV spectral-stripe can contaminate the FUV spectral-stripe and vice versa. This becomes particularly detrimental at spectral rows where one spectral-stripe is relatively dim while the other is relatively bright, where the scattered fraction from the brighter stripe rivals the unscattered signal in the dimmer stripe.

3.5. Linearity Correction

The CIS115 CMOS sensor is highly linear across most of its dynamic range, but becomes non-linear under high illumination. CSOL was calibrated over a range of optical intensities in order to characterize this non-linearity and derive a linearity correction. Calibrations were made at seven synchrotron-beam currents, ranging from 54 mA to 540 mA. Figure 8a shows the average electrons per pixel across the FUV spectral-stripe for the seven calibrations, with the corresponding beam currents annotated on the figure. Figure 8b shows the response-function $[R(\lambda, \theta, \phi)]$ in synchrotron-beam-current units for the seven calibrations, where the color code is the same as that defined in Figure 8a. If the instrument behaves linearly with intensity, $R(\lambda, \theta, \phi)$ will be invariant with incident flux. The fact that calibrations at

the two highest intensities (485 and 540 mA) have markedly smaller response-functions indicates a non-linearity at high signal levels, where the detector produces fewer electrons than expected if the detector response were perfectly linear. An alternate visualization of this nonlinearity for a single wavelength is shown in Figure 8c, which shows the measured electrons versus synchrotron beam current at 160 nm with red asterisks and a linear fit to the five lowest beam currents is over-plotted with a dashed line.

We define a linear correction factor for a given electron count as the ratio of counts predicted by a linear fit of the five lowest beam currents to the measured value. For the example shown in Figure 8c, the correction factor at the measured 2100 electrons s^{-1} would be $\approx 2200/2100 = 1.048$ from the data for the 540 mA calibration. Correction factors are found at every detector pixel row (i.e. wavelength bin) using the set of seven linearity calibrations to generate the scatter plot shown with black asterisks in Figure 8d. These data are fit to a quadratic equation with resulting coefficients, $2.8 \times 10^{-8} M^2 - 3.1 \times 10^{-5} M + 1.006$, to estimate the required linearity correction for a given detector intensity. During data processing, the data are scaled using this correction to remove the non-linearity.

3.6. Spectral Calibration

SURF III was used to calibrate the instrument response-function, $[R(\lambda, \theta, \phi)]$ by solving Equation 1 where the lefthand side of the equation is the precisely known synchrotron irradiance and the corrected counts $[C]$ were measured and corrected using the methods described above, leaving $R(\lambda, \theta, \phi)$ as the only unknown. The standard SURF III beam intensity decays rapidly at high intensities due to a process known as Touschek scattering, which can be mitigated by applying a radio frequency field to the electrons in the synchrotron ring (Arp et al., 2000). This process of stabilizing the beam intensity, referred to as "fuzzing", broadens the optical-beam cross-section, where a stronger fuzz results in higher stability, a broader beam cross-section, and less accuracy. A fuzz resulting in a 6 mm horizontal beam cross-section (hereafter referred to as "6 mm fuzz") is used at SURF III to reduce the beam decay with minimal impact on the irradiance uncertainty. During the initial CSOL calibrations, an unusual interference effect, described next, was observed with an un-fuzzed calibration beam, resulting in all calibrations being made using a 6 mm fuzzed beam.

Figure 9 shows the interference patterns observed on the CSOL detector when an un-fuzzed calibration beam is used, in units of the fractional difference from the 6 mm fuzzed calibration beam. Examples are shown at three different roll positions (0°, 45°, and 90°), indicating a sensitivity to the beam polarization relative to the CSOL entrance slit. Additionally, the average of the 0° and 90° calibrations is shown in the top panel. Note that the 6 mm fuzzed calibration beam shows no interference pattern, an example of which can be seen in Figure 5a, implying that the apparent periodic structure coincides with the un-fuzzed beam. The origin of this interference pattern is unknown and prior occurrences of this phenomena were not observed during the calibrations of the *EUV Variability Experiment* (EVE: Hock et al., 2012) and *Solar EUV Experiment* (SEE: Eparvier et al., 2001) instruments calibrated by co-author Woods at the same beam line, nor has this phenomenon been previously observed in other instruments by staff physicists at SURF III.

CSOL has a novel grating geometry that directs the zeroth-order beam from the MUV slit to the FUV slit and vice versa creating an etalon for any light retro-reflected from the backside of the slit plane or backside of the filter, and the etaloning could possibly cause the observed interference fringes. Another source of etaloning could be between the filter and reflective front-side of the slit plane. However, it is not clear why the fuzz would suppress the

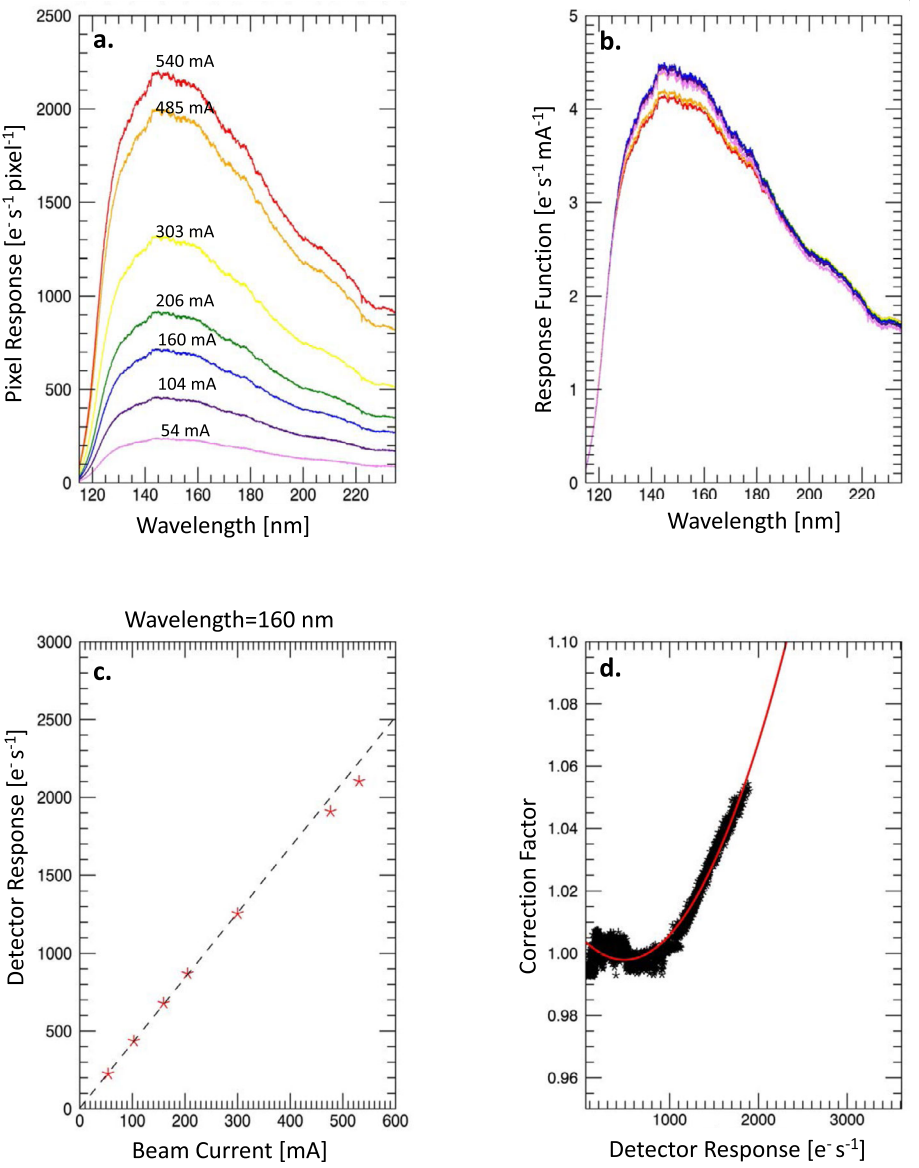

Figure 8 CSOL linearity calibration. **(a)** Detector response at the seven beam currents used for the linearity calibration. **(b)** Corresponding response-functions; the color code matches that in Panel **a**. **(c)** Example linearity at 160 nm showing non-linearity at high electron production rates. **(d)** The resulting linearity correction factor data and quadratic fit (*red*).

etaloning. One possibility is that the fuzz injects a degree of incoherence, although this explanation is inconsistent with prior reports of the nominal un-fuzzed beam being incoherent (Arp et al., 2000).

Polarization tests indicate that the deleterious impact of the interference effect on the instrument calibration is reduced but not completely removed with 6 mm fuzz. The Fresnel

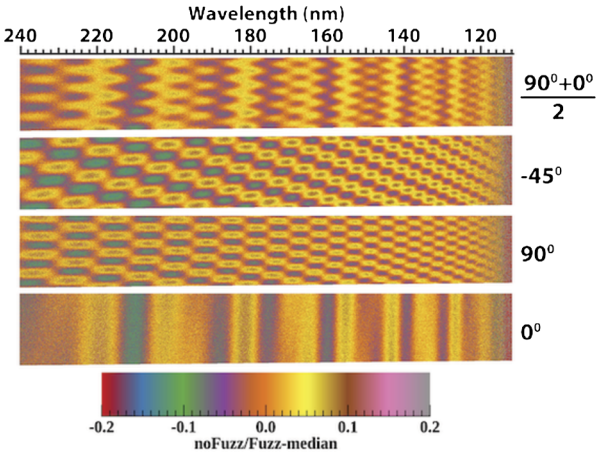

Figure 9 Interference pattern observed when an unfuzzed beam is used to calibrate CSOL. *From bottom to top* the interference pattern at 0°, 90°, and −45° roll orientation. *Top row:* The average of the interference patterns from the 90° and 0° orientations.

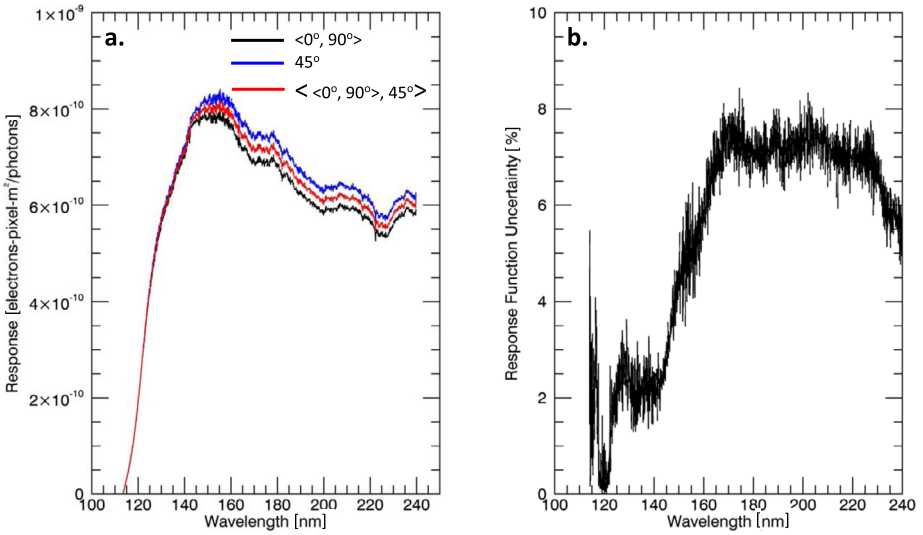

Figure 10 Response function measurements. **(a)** Mean of 0° and 90° roll position response-functions (*black*) compared with that from the 45° orientation (*blue*). The nominal response-function is the mean of the *blue* and *black* curves and shown in *red*. **(b)** Response-function uncertainty.

equations maintain that the response-function measured at a 45° polarization angle will be equal to the average response-function measured at the 0° and 90° polarization angles. Figure 10a shows the 0° and 90° mean response-function with a black curve and the response-function measured at 45° with a blue curve, revealing that the two are equal at shorter wavelengths but diverge at longer wavelengths. From Figure 9, it is apparent that the fringe size in the dispersion direction gets smaller at shorter wavelengths. As such, impacts of the interference effect on the calibration are smaller at shorter wavelengths, which may explain why the agreement between the 0° and 90° mean response-function and the 45° response-function is better at shorter wavelengths. The mean of these two response-functions is chosen to be the calibrated response-function, and it is shown with a red curve in Figure 10a, and their

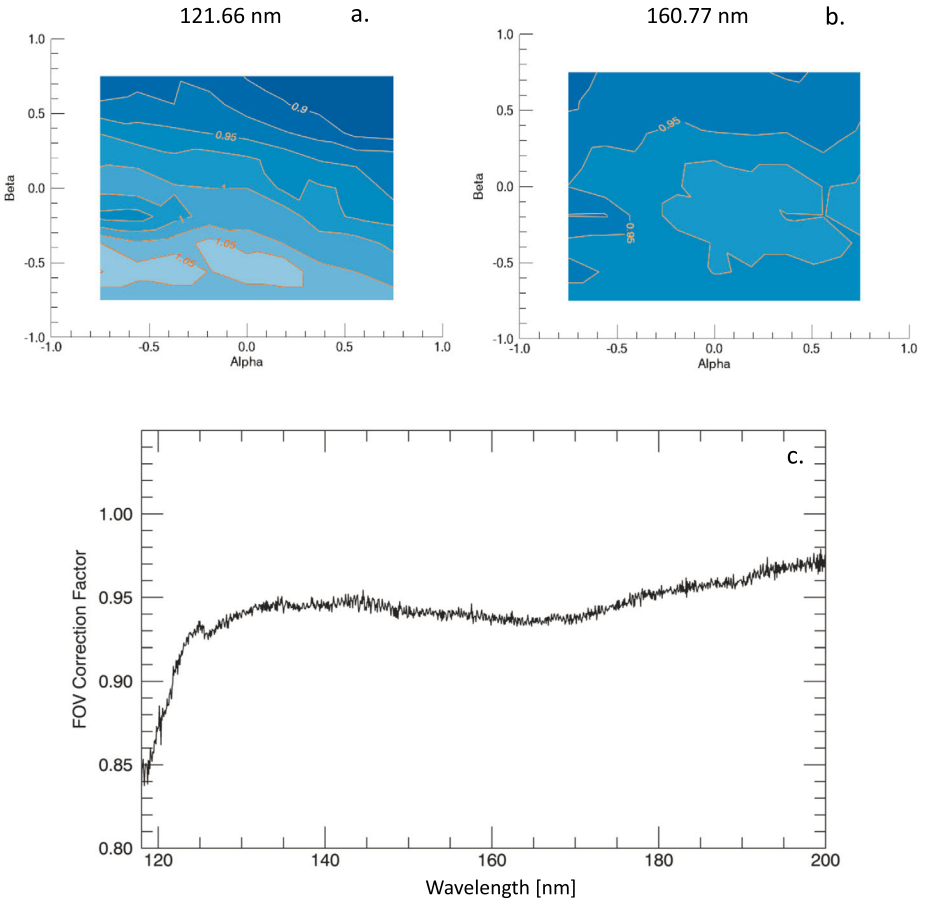

Figure 11 The field-of-view correction. Example field-of-view maps at **(a)** 121.66 nm and **(b)** 160.77 nm. **(c)** Final field-of-view correction as a function of wavelength for the solar measurements.

absolute difference is taken to be the response-function uncertainty, and it is shown in Figure 10b. The uncertainty is near 0.2% at 121.6 nm, near 2% between 125 nm and 140 nm, and increases to $\approx 7\%$ between 140 nm and 150 nm, where it remains through 220 nm. Note, this is considerably larger than the nominal SURF III uncertainty of 0.1%.

3.7. Field of View Correction

A field-of-view (FOV) correction is applied to account for the rocket-flight pointing and the spatial extent of the Sun, using FOV map data collected at SURF III. The FOV map was generated by stepping the SURF beam across 1.5° in pitch and yaw on a 9×9 grid (0.188° grid sampling) centered at the nominal-calibration center point, resulting in a total of 81 measurements. The FOV maps are divided by their value at (0°, 0°), so that they directly provide a scaling factor to adjust the calibration measured at (0°, 0°) to other angular locations. Examples of the FOV maps at two wavelengths are shown in Figure 11a and Figure 11b. The FOV maps are fit to a plane near the rocket-flight pointing angle at (0.8°, 1.54°), and this plane is convolved with a 0.53° disk centered at the rocket-flight pointing

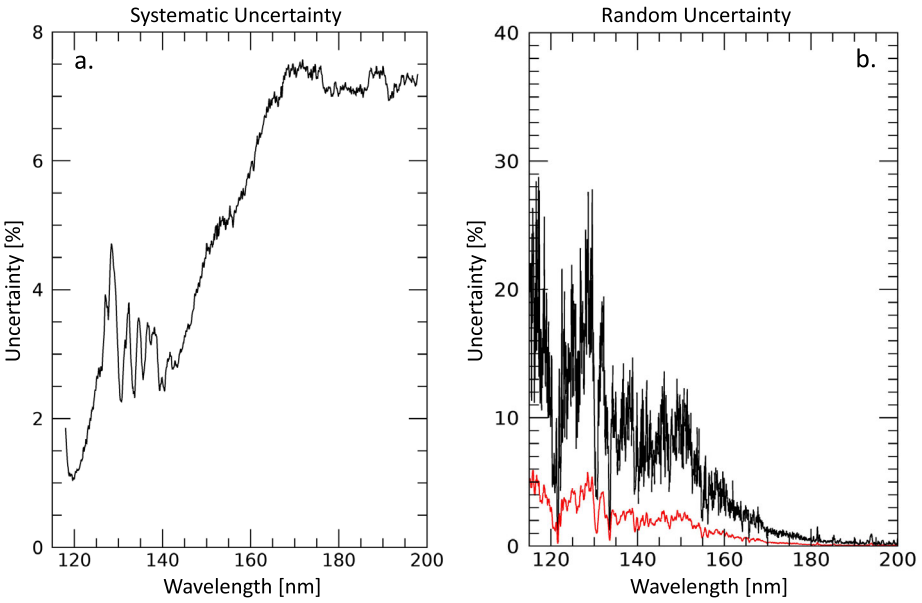

Figure 12 **(a)** Total combined systematic uncertainty from the SURF III calibration. **(b)** Random uncertainty during the 18 June 2018 rocket-flight for a single detector image (*black*) and after averaging the 16 detector images used to determine the solar irradiance (*red*).

angle. Since each pixel row has a unique FOV map, this process is repeated at every pixel row, generating an FOV correction factor as a function of wavelength, shown in Figure 11c. The field-of-view correction uncertainty is estimated from the spread of the FOV correction factors over a small (≈ 2 nm) wavelength intervals to be $\approx 0.5\%$. We estimate an additional systematic uncertainty due to the data interpolation scheme from the total change of the FOV correction factor across nine grid points, which is ≈ 0.15 across the measured FOV or 0.017 per grid point. From this, we conservatively carry an additional 1.7% systematic uncertainty due to the FOV correction.

3.8. Total Combined Uncertainty

The instrument uncertainty consists of two fundamental components: the systematic uncertainty due to the instrument calibration (i.e. the accuracy) and the random uncertainty due to measurement noise during the rocket-flight (i.e. the precision). The major source of the systematic uncertainty is from the response-function calibration, shown in Figure 10b. Other contributors to the systematic uncertainty include counting uncertainty (during the response-function calibration), the linearity-correction uncertainty, the scattered-light correction uncertainty, and the FOV correction uncertainty. The counting uncertainty in fractional units is $1/\sqrt{N_\mathrm{e} \times N_\mathrm{p}}$, where N_e is the average number of electrons measured per pixel and N_p is the number of pixels that are averaged in the cross-dispersion direction, which is approximately 250. The counting uncertainty exceeds 1% for signal levels of 40 electrons or less. For the response-function calibration, the counting uncertainty adds an additional $\approx 0.6\%$ at 120 nm and 0.4% or less above 125 nm. The linearity correction uncertainty is 0.03% and calculated by taking the standard deviation of the fit and data difference shown in Figure 8.

Figure 12a shows the total combined systematic uncertainty, found by adding in quadrature the (linearly independent) uncertainty components listed in the preceding paragraph. As expected, the total combined systematic uncertainty generally follows the shape of the response-function uncertainty, with the grating-scatter correction uncertainty adding structure between 120 and 140 nm. The smaller uncertainty terms contribute to an offset, keeping the uncertainty above 1% at all wavelengths. The best instrument performance is below ≈ 150 nm, where the uncertainty is less than 5% and equal to 2.89% on average.

Figure 12b shows the random uncertainty during the rocket-flight. The uncertainty for a single detector image is shown in *black* and that for the average of sixteen images used to determine the solar irradiance is shown in *red*. Coincidentally, it trends with wavelength opposite to that of the systematic uncertainty, being generally higher ($\approx 5\%$) at shorter wavelengths, where the measured signal is lower, and it approaches zero at longer wavelengths, where the measured signal is higher. The random uncertainty at the bright H Lyman-α line at 121.6 nm is $\approx 0.5\%$. The total uncertainty is estimated by summing the systematic and random components and is approximately $\approx 3\%$ at the H Lyman-α line, 4% at the other bright lines, and 7% in between the bright lines, except for the low-signal region between 122 nm and 130 nm, where it is approximately 10%. Note that the uncertainty in the 122 to 130 nm range is likely even higher due to limitations of the grating-scatter correction in this region. We estimate the uncertainty in the 122 to 130 nm range to be $\approx 30\%$ from the relative variance of bins spanning this range.

4. Rocket Flight Measurements

CSOL launched onboard NASA sounding rocket 36.336 from White Sands Missile Range, New Mexico, on 18 June 2018, at 19:00:00 UT, for a flight lasting 935 seconds. During this flight, CSOL made measurements at or above 120 km for 342 seconds and reached a maximum altitude of 293 km. The solar 10.7 cm radio flux ($F_{10.7}$) for this flight was 76.3 SFU, indicating low solar activity. The methods described in the preceding section were used to process 17 solar and 20 dark measurements, sampled with 10-second integrations. The resulting spectrum at full spectral resolution and sampling is shown in Figure 13 in black, and the daily average Version 18 SORCE/SOLSTICE spectrum filtered to 0.476 nm resolution is over-plotted in red. It is important to note that the SOLSTICE calibration was implemented independently of the CSOL data and no scaling was done to the CSOL spectrum to improve agreement with SOLSTICE.

Figure 14 shows subsets of the spectrum in Figure 13 for detailed evaluation. CSOL data are shown in black and SOLSTICE data in red. Individual bins at CSOL's full resolution are shown with points, and the lines show the data binned at 1-nm sampling. This figure also includes the upper and lower uncertainty bounds of the CSOL measurements shown in gray. The dominant feature in Figure 14a is the H Lyman-α line at 121.6 nm. Considering the bin centered at 121.5 nm, CSOL is 4.7% brighter than SOLSTICE, larger than the expected 2% uncertainty of CSOL alone (the implications of the SORCE uncertainty are discussed in Section 5).

The CSOL grating-scatter correction over-corrects the scatter in the wings of the Lyman-α line and results in a number of bins having negative irradiance (which is set to zero, as discussed in Section 3.4). This is why there are some missing CSOL data points, most pronounced in the 122.5 nm bin, and these zeroed full-resolution bins bias the 1-nm averaged bins low from 122 nm to 129 nm.

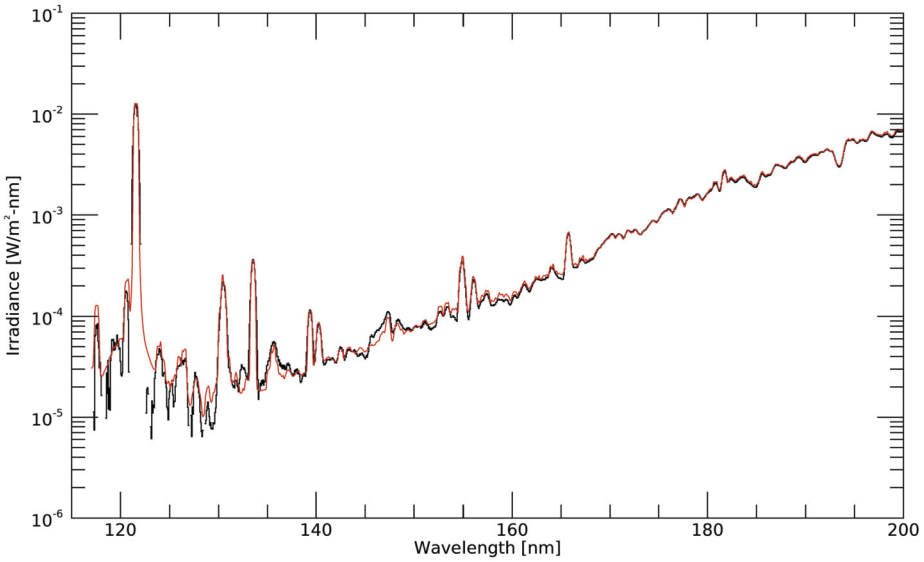

Figure 13 The FUV solar spectrum measured by CSOL at full spectral resolution (*black*). SORCE/SOLSTICE data for the corresponding day are over-plotted in *red*.

There is disagreement between the magnitudes of the brightest two lines in Figure 14b, with the 130.4 nm and 130.9 nm Si II emissions in the 130.5 nm bin being 6.2% brighter in the SOLSTICE spectra and the 133.5 nm and 133.6 nm C II emissions in the 133.5 nm bin being 9.5% brighter in the CSOL spectra. Also notable over this wavelength range is the 147.3 nm S I emission in the 147.5 nm bin, which is 15.6% brighter in CSOL than in SOLSTICE. The agreement between the CSOL and SOLSTICE spectra is excellent between 150 nm and 199 nm, where the spectra generally agree within the CSOL uncertainty from 150 nm to 199 nm, as can be seen in Figures 14c and d.

5. Discussion and Conclusions

When considering the whole spectrum, there is very good agreement between CSOL and SOLSTICE, indicating no major relative biases in the CSOL and SOLSTICE calibration. Differences between the CSOL and SOLSTICE measurements exist, most notably at the bright emission lines. The differences in the shape of the H Lyman-α line suggest that differences in the grating-scatter correction may contribute to the differences in the peak intensity, with the SOLSTICE spectra showing a broader fall off in signal away from 121.5 nm.

SORCE/SOLSTICE has a beginning-of-mission accuracy of 2 – 6%, with the accuracy varying from 6% near 130 nm to 2% near 150 nm (see Figure 10 in Snow et al., 2005a). The calibration uncertainty is estimated to increase by 0.2% year^{-1} from 2003 (Snow et al., 2022), and reach a level of 3% at the time of the CSOL measurements, so that the SOLSTICE total uncertainty at the time of the CSOL measurements ranges from $\approx$ 3.6 – 6.7%. Much of the differences between SOLSTICE and CSOL fall within the range of the combined instrumental uncertainties, including H Lyman-α, but discrepancies in other spectral bins, such as the 147.5 nm, exceed that of the combined instrumental uncertainties. To better

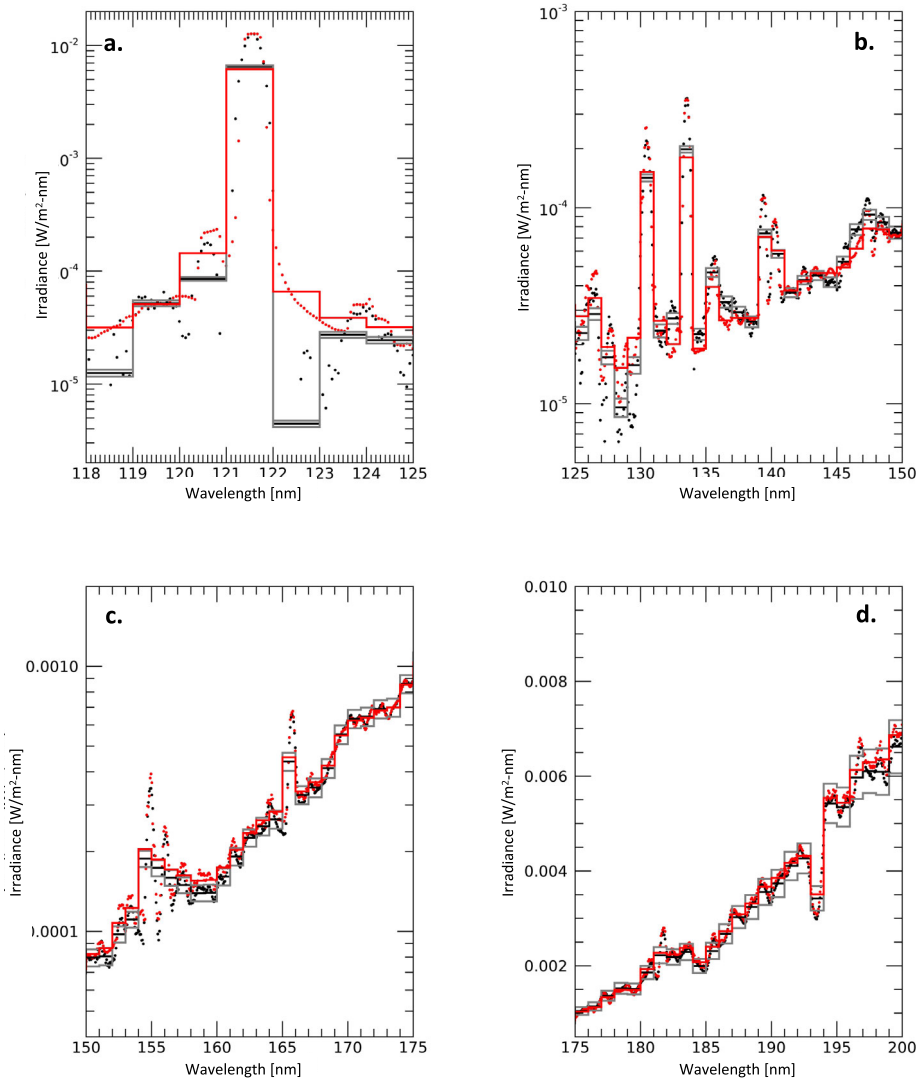

Figure 14 Solar spectra measured by CSOL (*black*) and uncertainty bounds (*gray*) over four wavelength intervals. SORCE/SOLSTICE data for the corresponding day is over-plotted in *red*. *Lines* correspond with one-nm binned data and *dots* correspond with data at the CSOL native spectral resolution.

understand the source of these discrepancies, line ratios are computed for CSOL and SOLSTICE and compared with SOLSTICE measurements during the prior solar cycle, when the SORCE calibration is expected to be more certain, at a similar level of solar activity. The bin ratios considered are 130.5 nm/133.5 nm and 139.5 nm/147.5 nm and are reported in Table 1. Ratios computed from SORCE/SOLSTICE and TIMED/SEE measurements made on 25 February 2006, when the $F_{10.7}$ flux was at comparable levels as that during the CSOL rocket flight, are also reported. The SOLSTICE and SEE ratios tend to be in reasonable agreement while the CSOL measurements are the outliers. The discrepancy in these line ratios in CSOL versus SOLSTICE and TIMED is difficult to explain. Given the spectral

Table 1 Comparison of two selected line ratios measured by CSOL, SORCE/SOLSTICE and TIMED/SEE.

Measurement	130.5/133.5	Precision	139.5/147.5	Precision
CSOL	0.71	7.1%	0.82	4.6%
SOLSTICE 2018	0.83	4.7%	0.94	8.1%
SOLSTICE 2006	0.85	2.3%	0.93	4.4%
SEE 2006	0.81	5.3%	0.91	7%

proximity and comparable intensities of these lines, unidentified systematic errors in the instruments calibration should be mostly controlled for. Furthermore, given the similarities in the CSOL and SOLSTICE uncertainties over this wavelength range, there is no obvious reason to favor the calibration of one instrument over the other.

In conclusion, the CSOL calibration rocket under flight has validated the final calibration of the SOLSTICE instrument. At wavelengths above 150 nm, the agreement between CSOL is excellent and well within the combined instrumental uncertainty. The CSOL measurements also support the existing understanding of the absolute solar H Lyman-α irradiance. Some unexplained discrepancies in line ratios exist in the 130 nm – 150 nm range that warrant further future study. While the final SOLSTICE data products (Snow et al., 2022) do not directly incorporate the CSOL underflight calibration results, they clearly benefit from this validation with the CSOL measurement. Additionally, the CSOL rocket-flight has demonstrated the capability of a compact FUV spectrograph to make state-of-the-art solar spectral irradiance measurements with uncertainties comparable to those of the historical data record. At the time of this writing, the CSOL spectrograph is being retrofitted for the NASA *Occultation Wave Limb Sounder* (OWLS) instruments to fly on the INSPIRESat3 microsatellite (1ft^3), where it is intended to measure solar disk spectral radiance while making solar-occultation measurements of the lower and middle thermosphere (Thiemann et al., 2018).

Acknowledgments Sadly, Mitchell Furst passed away on 13 March 2022, during the preparation of this manuscript. The remaining co-authors are thankful for his tireless effort and significant contribution calibrating many space-based EUV irradiance sensors over nearly five decades. He will be missed.

Author contributions E. Thiemann wrote the main manuscript and implemented final post-flight calibration. J. Harder made substantial writing contributions and led the development and pre-flight calibration of the instrument. T. Woods provided senior advising and led the rocket flight of the instrument. M. Snow supported instrument calibration and in particular comparisons with SORCE/SOLSTICE. M. Klapetzky designed the instrument optics, and supported calibrations and alignments. M. Triplett supported calibrations and alignments. A. Sims designed the instrument electronics. S. Penton designed calibration software. M. Furst operated the synchrotron calibration facility.

Declarations

Competing interests The authors declare no competing interests.

References

Arp, U., Friedman, R., Furst, M.L., Makar, S., Shaw, P.-S.: 2000, SURF III-an improved storage ring for radiometry. *Metrologia* **37**, 357.

Brown, S.W., Eppeldauer, G.P., Rice, J.P., Zhang, J., Lykke, K.R.: 2004, Spectral irradiance and radiance responsivity calibrations using uniform sources (SIRCUS) facility at NIST. In: Barnes, W.L., Butler, J.J. (eds.) *Earth Observing Systems IX*, *Proc. Soc. Photo-Opt. Instrum. Eng. (SPIE)* **5542**, 363. DOI.

Eparvier, F.G., Woods, T.N., Ucker, G.J., Woodraska, D.L.: 2001, TIMED solar EUV experiment: preflight calibration results for the EUV grating spectrograph. In: Siegmund, O.H.W., Fineschi, S., Gummin, M.A. (eds.) *UV/EUV and Visible Space Instrumentation for Astronomy and Solar Physics*, *Proc. Soc. Photo-Opt. Instrum. Eng. (SPIE)* **4498**, 91. DOI.

Hayat, G., Flamand, J., Lacroix, M., Grillo, A.: 1975, Designing a new generation of analytical instruments around the new types of holographic diffraction grating. *Opt. Eng.* **14**, 420.

Hock, R., Chamberlin, P., Woods, T., Crotser, D., Eparvier, F., Woodraska, D., Woods, E.: 2012, Extreme ultraviolet variability experiment (EVE) multiple EUV grating spectrographs (MEGS): radiometric calibrations and results. *Solar Phys.* **275**, 145.

McClintock, W.E., Snow, M., Woods, T.N.: 2005, Solar-stellar irradiance comparison experiment II (SOLSTICE II): pre-launch and on-orbit calibrations. *Solar Phys.* **230**, 259. DOI. ADS.

NIST: 2018, NIST Ultraviolet Spectrum of Platinum Lamp. Technical report, U.S. Department of Commerce, National Institute of Standards and Technology. DOI.

Rottman, G.: 1988, Observations of solar UV and EUV variability. *Adv. Space Res.* **8**, 53.

Rottman, G.: 2005, The SORCE mission. *Solar Phys.* **230**, 7. DOI. ADS.

Rottman, G.J., Woods, T.N., Sparn, T.P.: 1993, Solar-stellar irradiance comparison experiment 1: 1. Instrument design and operation. *J. Geophys. Res., Atmos.* **98**, 10667.

Snow, M., McClintock, W.E., Rottman, G., Woods, T.N.: 2005a, Solar stellar irradiance comparison experiment II (solstice II): examination of the solar stellar comparison technique. *Solar Phys.* **230**, 295. DOI. ADS.

Snow, M., Mcclintock, W.E., Rottman, G., Woods, T.N.: 2005b, Solar-stellar irradiance comparison experiment II (SOLSTICE II): examination of the solar-stellar comparison technique. In: *The Solar Radiation and Climate Experiment (SORCE)*, Springer, Berlin, 295.

Snow, M., McClintock, W.E., Woods, T.N., Elliott, J.P.: 2022, SOLar-STellar irradiance comparison experiment II (SOLSTICE II): end-of-mission validation of the SOLSTICE technique. *Solar Phys.* **297**, 1.

Thiemann, E., Snow, M., Chandran, A., Woods, T., Harder, J., Pilinski, M., Eparvier, F.G., Greer, K.: 2018, The Occultation Wave Limb Sounder (OWLS) on INSPIRESat-3. In: *42nd COSPAR Scientific Assembly* **42**, C2.

Woods, T.N., Rottman, G.J., Ucker, G.J.: 1993, Solar-stellar irradiance comparison experiment 1: 2. Instrument calibrations. *J. Geophys. Res., Atmos.* **98**, 10679.

Woods, T.N., Wrigley, R.T., Rottman, G.J., Haring, R.E.: 1994, Scattered-light properties of diffraction gratings. *Appl. Opt.* **33**, 4273.

Woods, T.N., Chamberlin, P.C., Harder, J.W., Hock, R.A., Snow, M., Eparvier, F.G., Fontenla, J., McClintock, W.E., Richard, E.C.: 2009, Solar irradiance reference spectra (SIRS) for the 2008 whole heliosphere interval (WHI). *Geophys. Res. Lett.* **36**, L01101.